Reconfigurable Photonics on a Glass Chip

I. V. Dyakonov,[1,2,*] I. A. Pogorelov,[1,2] I. B. Bobrov,[1,2] A. A. Kalinkin,[1,2] S. S. Straupe,[1,2] S. P. Kulik,[1,2] P. V. Dyakonov,[3] and S. A. Evlashin[4]

[1] *Faculty of Physics, M. V. Lomonosov Moscow State University, Leninskie Gory 1, Moscow 119991 Russia*

[2] *Quantum Technologies Centre, M. V. Lomonosov Moscow State University, Leninskie Gory 1, Moscow 119991 Russia*

[3] *Skobeltsyn Institute of Nuclear Physics, M. V. Lomonosov Moscow State University, Leninskie Gory 1, Moscow, 119991 Russia*

[4] *Center for Design, Manufacturing and Materials, Skolkovo Institute of Science and Technology, 3 Nobel Street, Moscow 143026, Russia*

(Received 12 May 2018; revised manuscript received 27 July 2018; published 19 October 2018)

The reconfigurability of integrated photonic chips plays a key role in current experiments in the area of linear-optical quantum computing. We demonstrate a reconfigurable multiport interferometer implemented as a femtosecond-laser-written integrated photonic device. The device includes a femtosecond-laser-written 4×4 multiport interferometer equipped with 12 thermo-optical phase shifters, making it a universal programmable linear-optical circuit. We achieve a fast switching time for a single nested Mach-Zender interferometer of ~ 10 ms and quantitatively analyse the reconfigurability of the optical circuit. We believe that our results will improve the current state of quantum-optical experiments utilizing femtosecond-laser-written photonic circuits.

DOI: 10.1103/PhysRevApplied.10.044048

I. INTRODUCTION

The quest to build a large-scale linear-optical quantum computer implies the development of miniature, stable, and precise optical components. The remarkable success of the microelectronics industry proves the immense efficiency of integrated-device fabrication and dictates the future trend for quantum-photonic device engineering. Since the pioneering work [1], the integrated photonic approach has firmly retained its leadership in precision quantum-optical experiments [2,3], optical quantum computing [4], and quantum simulation [5]. Recent works [6] have also demonstrated the potential of adopting standard silicon photonic technologies for quantum applications, ensuring compatibility with modern CMOS fabrication lines.

Along with stability and precision, the integrated photonic technology provides a toolset for reconfigurable circuit fabrication, endowing the experimenter with the capacity to perform numerous experiments with a single device. Recently, quantum-computing experiments have been demonstrated on reconfigurable platforms [7–9], proving their potential for realizing completely different experimental settings with a single device [4]. Reconfigurability provides enough freedom to augment linear-optical quantum-computing experiments with machine-learning algorithms [8,9], paving the way for more sophisticated applications for devices of increased complexity.

Currently, the most advanced reconfigurable integrated photonic chips are fabricated using lithographic technology [6], providing the best possible precision of elementary components [10], miniaturization [11], and the fastest low-loss switching [12,13]. Several different optical architectures have been realized using this technology [4,5,14–16]. Furthermore, tunable optical integrated devices are designed and fabricated for many purposes, such as optical phased arrays [17], optical interconnects for microprocessors [18], signal processing [19], and others.

Recently, the femtosecond-laser-writing technology (FSLW) has established itself as a flexible tool for rapid prototyping of integrated photonic circuits, which is especially valuable for laboratory experiments, where the fabrication time is crucial. FSLW provides low-loss waveguide writing regimes for a wide variety of wavelengths from the visible to the telecom range [20–22]. Waveguide fabrication is possible in glasses, crystals, nonlinear materials, etc. [23]. FSLW enables polarization-state manipulation capabilities [24,25] and essentially three-dimensional (3D) waveguide circuit design [26]. The FSLW technology in the current quantum-optical scope provides a versatile tool for the processing of complex quantum states of light encoded in different degrees of freedom on the integrated photonic platform. For example, it has been applied for the

*iv.dyakonov@physics.msu.ru

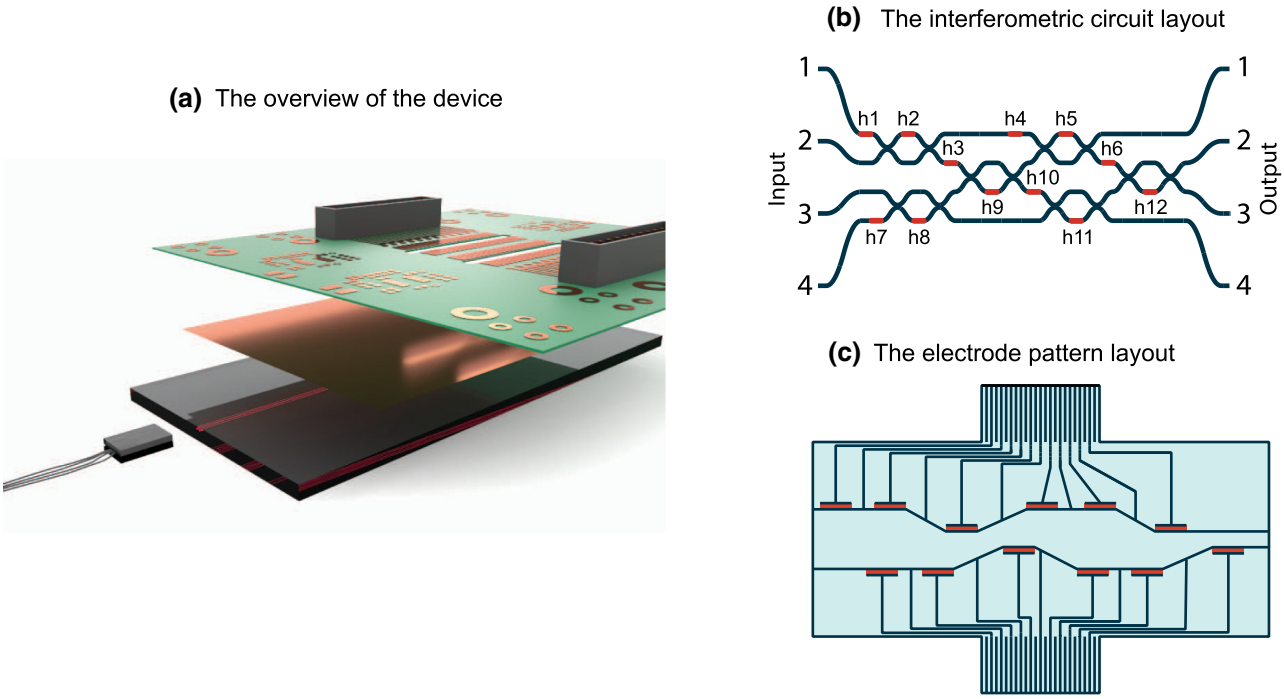

FIG. 1. (a) An overview of the fabricated device. (b) A schematic of the waveguide circuit written in the chip. For details of the geometry, see Appendix A. (c) An illustration of an electric pattern engraved in the metal film sputtered on the top surface of the chip. The drawing is not to scale.

characterization of hyperentangled path-polarization states [27] and further development of the active FSLW technology may significantly contribute to the on-chip manipulation of such states. One of the key advantages of this technology in comparison with lithography is its flexibility and very fast and inexpensive technological process.

Active thermo-optically adjustable elements have recently been introduced to the FSLW fabrication process [21,28] and several quantum-optical experiments have been performed with reconfigurable laser-written circuits [27,29]. However, a fully reconfigurable device, capable of realizing universal unitary transformations, has not been demonstrated so far. All previously demonstrated devices have included at most two consecutive thermo-optical phase shifters [29]. A modular architecture was suggested recently to enable assembly of such larger universal interferometers from smaller modules [30] but the electrode imprinting process used still required lithographic techniques. In this work, we demonstrate the fabrication process of a fully reconfigurable multiport interferometer using FSLW only. The electrodes are engraved using the same facility as the waveguides and the only step performed outside the optical laboratory environment is the metallization of the chip surface. This approach was pioneered in Ref. [21], but we improve it significantly in order to fit more thermo-optical elements on a single sample. Our device is capable of realizing a universal special unitary group of degree 4 [SU(4)] transformation, which is the largest unitary realized with a fully FSLW chip so far. Moreover, we improve the switching time of the phase shifters by 2 orders of magnitude, reaching the level of 10 ms. The performance of the device, including cross talks between heaters, is thoroughly characterized and an adaptive algorithm is introduced to tune the unitary for the desired output.

II. FABRICATION

We design the optical circuit of the reconfigurable chip using a unitary-matrix factorization algorithm developed in Ref. [31]. The key benefits of this elaborated procedure compared to the well-known Reck design [32] are the more compact footprint and the symmetric effect of propagation loss throughout the beam-splitter mesh. The latter feature endows the symmetric beam-splitter layout with greater robustness to loss, which allows for the fabrication of optical circuits of greater depth without a drastic reduction in fidelity. To achieve reconfigurability in the proposed design, one needs to tune the transmission ratio of every beam splitter and the relative phase shifts between the different arms of the circuit (see Fig. 1). To satisfy these requirements, the beam splitters are replaced with Mach-Zender interferometers, with adjustment of the output intensity and phase distribution enabled by thermo-optical elements. The full topology of the optical circuit is shown in Fig. 1(b).

The integrated photonic circuit is fabricated with a femtosecond-laser-writing technology. We expose a fused silica sample ($100 \times 50 \times 5$ mm^3, JGS1, AGOptics) to 178 nJ laser pulses (400 fs duration) at a 3 MHz repetition rate. We use a second harmonic of an ytterbium fiber femtosecond-laser system (Menlo Systems Bluecut). The laser light, at 515 nm central wavelength, is focused using a 0.55 NA aspheric lens 20 μm below the surface. Smooth waveguiding structures are inscribed inside the volume of the sample by translating it along the desired trajectory at the constant feed rate of 0.01 mm/s with an air-bearing translation stage (AeroTech FiberGlide 3D). The details of the experimental setup can be found in Ref. [25]. The fabricated waveguides exhibit 0.8 dB/cm propagation loss. The inscribed structures exhibit a rather low refractive index contrast; thus we set the bending radius of the curved interferometer sections to be 80 mm to ensure negligible additional bending loss. This drawback is typical for all FSLW-fabricated waveguides and severely limits the scalability of the integrated optical circuits created with this technology. Therefore, a four-mode universal interferometer circuit is the maximal universal multiport that we could possibly fit to our samples. The geometrical parameters of the interferometer are summarized in Table II of Appendix A. The integrated circuit is written 20 μm below the surface to ensure a fast thermo-optic response. The quality of the optical waveguides written at small depth is significantly affected by the variance in the surface thickness. To eliminate that factor, we use 5-mm-thick slabs with the surface polished up to $\lambda/10$ at 633 nm flatness quality. After the optical circuit is written, the location of the interferometer is marked with alignment patterns. We use these markers to realign the position of the sample with the translation-stage coordinate frame, to engrave the heating elements at the required locations relative to the interferometer. The position of the markers can be restored with 1 μm precision. Lastly, the end faces of the chip are optically polished.

To create the heating elements on the chip, we deposit a metal NiCr film via a magnetron sputtering process. The sample is washed in an ultrasonic bath, in an oil-removal solution, and cleaned in ethanol afterward. It is preheated up to 150 °C to enhance the adhesive properties of the surface and a 1-μm-thick NiCr film is sputtered on the top surface of the sample. Next, we mount the chip back in the FSLW facility, realign it with the positioning-stage coordinate frame using the marker pattern, and engrave the electrode circuit with 50 nJ pulses at a 1 MHz repetition rate, focused with a 0.7 NA objective. The active heating parts of the fabricated electrodes are 3 mm long and 50 μm wide. The full electrode pattern as engraved is shown in Fig. 1(c). The heater resistance values vary between 350 and 1150 ohm. The large spread in the resistance values is the result of the variance in the metal film thickness and local film defects. An electrical interface with a homemade 12-bit digital constant current source is achieved via a printed circuit board (PCB) contacting the electrodes on the optical chip via thin metal springs. The whole assembly is mounted on the aluminum heat sink and the temperature of the chip is stabilized at 18 °C. An overview of the device assembly is given in Fig. 1(a).

III. DEVICE CHARACTERIZATION

We tested the device using a simple setup: laser light at 808 nm was injected in the chip through a butt-coupled single-mode v-groove fiber array; light on the output was collected using a multimode v-groove fiber array and sent to fiber-coupled photodiodes. The device performance is characterized by the precision of preparing the desired intensity distribution on the output and by temporal switching constants: t_1, the switching time of a single interferometer; and t_2, the time delay required for the whole system of electrodes to reach the equilibrium state. To measure the t_1 time, we apply a rectangular current pulse to heater h8 [see Fig. 1(b)] and observe an optical response of the circuit on output 4 using an oscilloscope. This signal allows us to extract the pulse response function of a single phase shifter, which is shown in Fig. 2(a). The optical response time t_1 is measured as a 10–90% rise time and is found to be different for the heating and the cooling processes: $t_1^h = 13$ ms and $t_1^c = 10$ ms. There are two main explanations for the radical improvement in switching time compared to [21,28]. First, we use thick 5 mm glass samples with $\lambda/10$ at 633 nm flatness, which allows us to write the waveguides closer to the surface. Second, the thermo-optical constant of the fused silica material is typically 3–5 times higher than for borosilicate glasses [33].

Next, we perform the phase vs current calibration for each heater to determine the 2π current thresholds. Figure 2(b) illustrates the intensity dependence on output port 3 while sweeping the current on heater h8 in 0.15 mA steps. A heuristic polynomial function $\phi(I)$ of the form

$$\phi(I) = \alpha + \beta I^2 + \gamma I^3 \tag{1}$$

provides an estimate of the 2π phase shift current and hence of the dissipated power. The fit of the experimental data provides an estimate of $\beta = (7.45 \pm 0.03) \times 10^{-3}$ rad/mA^2. To estimate the thermal cross talk manifested in parasite phase shifts induced by the neighboring heaters, we measure analogous dependencies while driving the heaters, which ideally should not affect the measured output. For example, Fig. 2(c) represents the output intensity pattern in port 1 with the input light injected in port 2 while the driving current is swept through heater h1, which, according to the design, should not modify the output intensity. However, due to a comparable inter-waveguide distance $d = 100$ μm and a heater width of $w = 50$ μm, the cross-talk effects are almost inevitable in

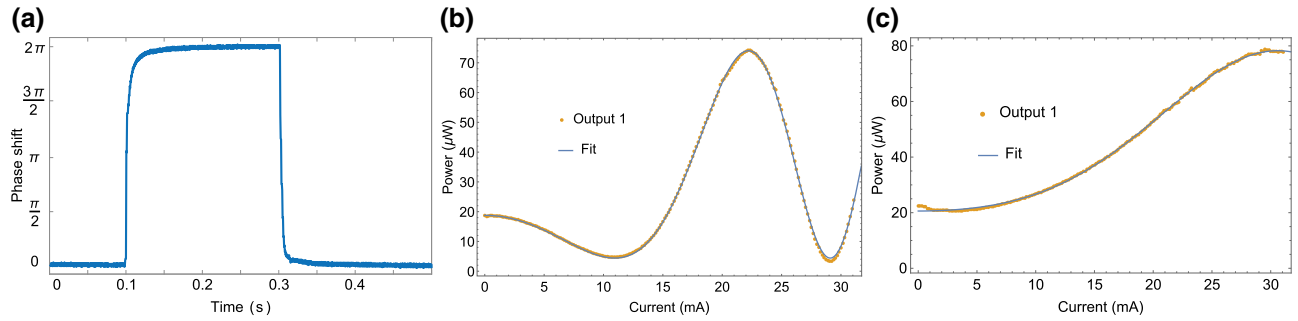

FIG. 2. (a) The response curve for the rectangular excitation current pulse applied to heater h8. (b) The calibration curve for heater h8. The interference pattern on output port 3 is measured while sweeping the control current through heater h8. (c) The observed cross-talk effect on output port 1 while sweeping the control current through heater h8.

such kinds of devices. The cross-talk rate is only several times smaller than β on average and should be taken into account.

IV. THE ADAPTIVE CIRCUIT TUNING

In principle, the multiport interferometer design implemented in our device enables arbitrary unitary transformations in the space of the guided modes [31]. The integrated photonic chips manufactured using a standard lithography process show better performance in terms of precision due to the highly repeatable technology of fabricating elementary photonic components, such as directional couplers, which play the central role in the overall precision of universal multiport integrated devices. Hence, the heater calibration provides all the necessary data to program the desired unitary transformation. The FSLW technological process in our laboratory environment provides a repeatability level on a scale of a few percent, which reduces the performance level and complicates the phase choice decision for the required optical configuration. Thus, in this work we use an adaptive approach to find the pattern of currents through the heating electrodes required to tune the optical circuit to generate the predefined output light distribution. In our experiments, we focus on tuning the device solely to reproduce a given intensity distribution between the output ports. Complete characterization of the unitary transformation requires full process tomography and will be reported elsewhere.

The idea of an adaptive thermo-optical circuit adjustment is to launch an optimization procedure, which tunes the phases φ_i of the corresponding phase shifters by changing the control currents I_i and, step by step, optimizes the output intensity distribution to the desired configuration. We use the following procedure to optimize and test the thermo-optical system performance:

1. Laser light is coupled to the ith input port.
2. Output light transmission S_j is measured for each of the four output ports. Here and in what follows, we use the notation S_j instead of S_{ij} for the output intensity, since the input waveguide is not varied during the procedure.
3. The control voltages are tuned by an optimization algorithm in order to minimize the difference between the measured output intensities $\propto S_j$ and the required ones $\tilde{S}_j$.
4. The procedure is stopped if the difference function between the desired and the measured intensity configurations is small enough. Otherwise, steps 2 and 3 are repeated.

A. The optimization step

The adjustment procedure consists of two main parts, the calculation of a difference function and an optimization algorithm, as described below.

1. The difference function

The goal of the adjustment procedure is to minimize the difference between the measured and the required normalized output configurations. We use an infidelity function [34] to quantify this difference:

$$1 - F = 1 - \left(\sum_{j=1}^{N} \sqrt{S_j \tilde{S}_j} \right)^2 . \tag{2}$$

The normalized intensities are the quantities calculated from the experimentally measured output light intensities I_j as follows:

$$S_j = \frac{I_j - I_j^{\mathrm{bg}}}{\sum_{j=1}^{4} (I_j - I_j^{\mathrm{bg}})}, \tag{3}$$

where I_j^{bg} is the background light intensity in channel j.

2. The optimization algorithm

The difference function (2) is determined by the 12 control currents as parameters. The global search algorithm

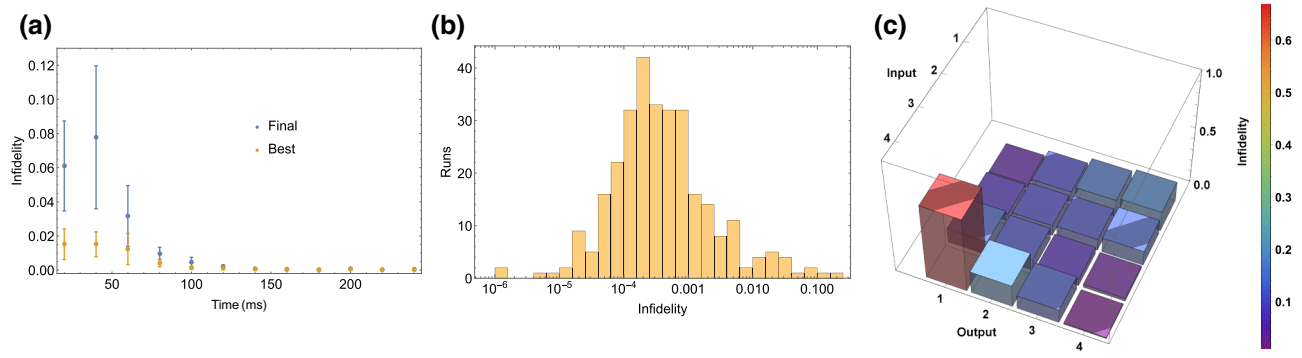

FIG. 3. (a) The infidelity values for the optimal configuration found during the tuning procedure (blue) and the infidelity values measured after resetting the configuration to the previously found optimal one once the tuning procedure is finished (red). The measurements indicate that even though the single interferometer responds rapidly to the driving current pulse, the whole circuit requires a longer time period to reach a steady state. We use the time delay between the sequential full reconfigurations, equal to 180 ms, to make sure that each measurement is taken in a thermally stable state. (b) The experimentally measured distribution of the infidelities of the output intensity distributions optimized to the randomly generated target intensity patterns. (c) The infidelity plot of all possible switching configurations of the device. In the worst-case scenario (elements 1–4), the light is traversing to the most distant output port and hence collecting the effect of more fabrication defects. The infidelity values of all switching configurations are summarized in Table I.

should be used for difference-function minimization to avoid convergence to a local minimum. Three search algorithms are tested: simultaneous perturbation stochastic approximation (SPSA) [35], particle swarm optimization (PSO) [36], and very fast simulated annealing (VFSA) [37]. The best search algorithm is supposed to provide the least difference-function value given a fixed number of measurements. The VFSA algorithm shows the best performance in the numerical simulations (see Appendix B) and is consequently used in the experiment.

First, we characterize the time required to reach an equilibrium state t_2. For this purpose, we run 300 optimization procedures with a fixed time t_2 between the consequent algorithm steps. We set the best found heater currents configuration after each optimization procedure has finished and measure the value of the difference function. Figure 3(a) illustrates the dependence of the difference-function value measured during the optimization search run (best) and after the search run is finished (final). The presented results clearly indicate that even though the switching time of a single Mach-Zender interferometer is fast enough at $t_1 = 10$ ms, the whole system of electrodes requires a time period that is an order of magnitude longer to stabilize the temperature distribution across the subsurface volume of the chip. In our setting, we use a $t_2 = 180$ ms time delay between the consecutive heater reconfigurations to ensure a steady-state output of the intensity measurements. This effect is mainly attributed to the sufficiently large heater surface areas (heater footprint 3×0.05 mm^2) required to induce a 2π optical phase shift. This is one of the limitations of the FSLW technology, which limits the achievable overlap between the temperature distribution generated by the heater and the optical waveguide core, since writing the waveguides closer than 10 μm to the top surface of the chip reduces their quality. We intentionally leave the heater sufficiently wide to prevent it from ripping apart while heating due to mechanical stresses induces by laser engraving of the electric pattern on the metal film. However, we believe that t_2 may be sufficiently improved by further adjustments of our fabrication process.

B. The reconfigurability test

To test the reconfigurability of the device, we perform a series of optimization procedures—tuning the device to operate as a switch, redirecting all the light from a given input port to a given output port, and tuning it to

TABLE I. The convergence results of the VFSA algorithm for the different input-output configurations in the intensity-switching mode. The infidelities averaged over 10 runs of the algorithm are shown.

		Output			
		1	2	3	4
Input	1	0.040 ± 0.006	0.097 ± 0.017	0.152 ± 0.018	0.176 ± 0.003
	2	0.066 ± 0.009	0.095 ± 0.014	0.103 ± 0.014	0.132 ± 0.081
	3	0.129 ± 0.004	0.103 ± 0.041	0.062 ± 0.007	0.027 ± 0.006
	4	0.669 ± 0.034	0.200 ± 0.041	0.122 ± 0.042	0.010 ± 0.002

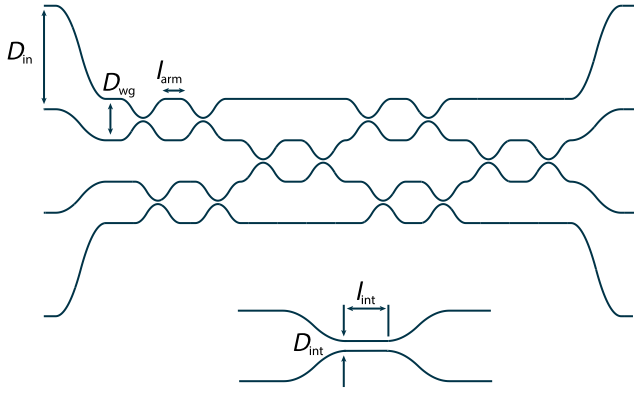

FIG. 4. The geometrical parameters of the multiport interferometric integrated circuit fabricated in this work.

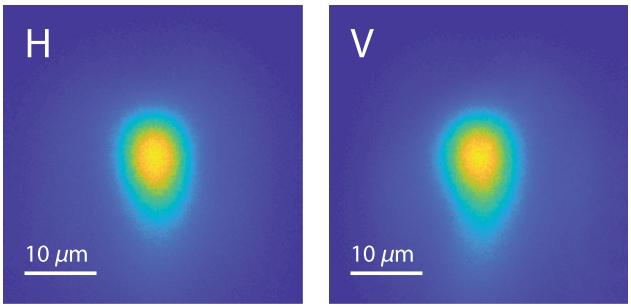

FIG. 5. The mode field profiles measured for horizontal and vertical-polarization states.

randomly selected target intensity distributions. The results are shown in Figs. 3(c) and 3(b), respectively. On average, finding the heater configuration corresponding to a randomly generated pattern turns out to be an easier task in our experimental setting due to the lower sensitivity to the background intensity collected by the output multimode fiber array.

Next, we test the device in the switching regime. The switching regime requires setting the intensities in three ports as close to zero as possible, which is sufficiently limited by the amount of the detected background scattering (mostly due to unguided laser radiation propagating inside the sample). The coupling of the chip output to the single-mode fiber array may significantly improve the performance of the optimizer in the switching regime. Figure 3(c) shows the results of optimizing the heater configuration in the intensity-switching mode. The worst-case scenario for the device under test corresponds to guiding the light toward the most distant output port and results in a sufficient quality reduction. We attribute this behavior to the impact of the interferometer writing imperfections, i.e., the limited interference visibility for the nested interferometers. For example, the infidelity value $(1-F)_{41} = 0.669 \pm 0.034$ indicates that the Mach-Zender interferometer controlled by heater h5 works worse than expected. One of the reasons for such poor behavior might be the order of writing of the circuit waveguides and the low feed rate $v = 0.01$ mm/s—the waveguide with input 1 and output 1 is written last in the fabrication sequence and due to the low feed rate, the time difference between writing the first and the last waveguides is approximately 8.5 h. During this period, either the exposure conditions could have changed slightly or dust particles could have contaminated the surface.

TABLE II. The integrated optical circuit geometry.

Curvature radius, R	80 mm
Input separation, D_{in}	250 μm
Waveguide separation, D_{wg}	100 μm
Interaction separation, D_{int}	8.57 μm
Interaction length, l_{int}	0 mm
Arm length, l_{arm}	2.5 mm

V. CONCLUSION

We present our results on the fabrication of a programmable multiport integrated optical circuit using the femtosecond-laser-writing technology. Our work demonstrates the possibility of producing fully reconfigurable interferometers with 10 ms switching time, which is an order of magnitude faster compared to all previously reported results [21,28]. We characterize the reconfigurablity of the device using classical input light and develop an adaptive procedure to tune the circuit in accordance with the desired configuration. Further developments should be dedicated to refining the device performance to meet the required precision to operate in the quantum regime, i.e., to set arbitrary unitary transformations with high fidelity. This goal requires better localization of the heated chip areas to reduce the cross-talk effects, enhancement of the replicability of the directional coupler fabrication, and possibly adjustment of the optimization procedure to account for the device process tomography at each algorithm step. Furthermore, development of the waveguide and heater fabrication technology and an appropriate choice of the optical substrate with a high thermo-optical coefficient combined with a thermal isolation approach, demonstrated in Ref. [28], may improve the t_1 and t_2 timing characteristics of such kinds of devices. From our point of view, the main problem in the current design of the electrodes is the metal film, which covers the whole surface of the chip and conducts heat from the thin stripes across the chip surface. Redesigning the electrode pattern and removing the excess metal from the surface should help to diminish the heat transfer across the chip surface and thus reduce the t_2 time.

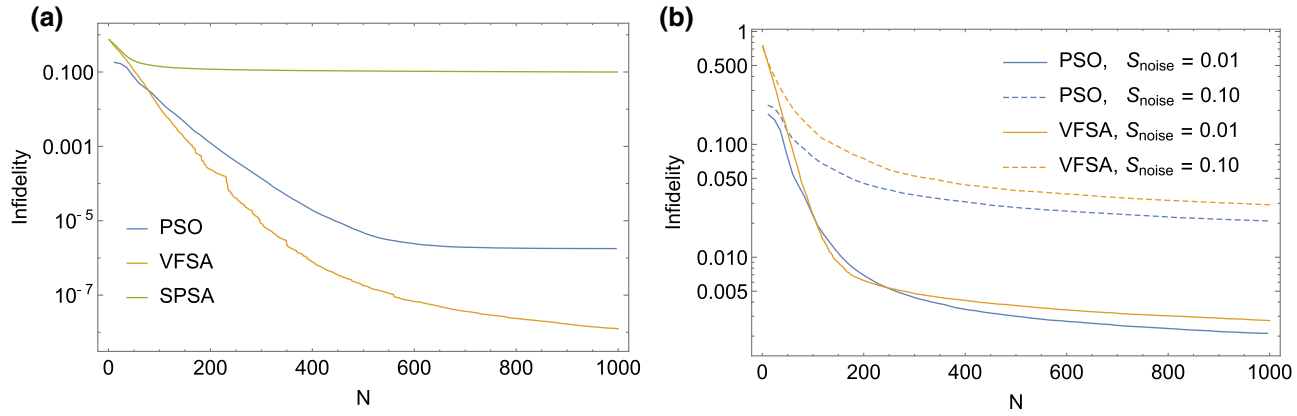

FIG. 6. The numerical simulations. The convergence of the different optimization algorithms to the target configuration $\tilde{S} = \{1, 0, 0, 0\}$. Infidelity is plotted as a function of the number of measurements N. The results are averaged over 1000 runs. (a) No noise; (b) virtual noise introduced.

However, even with the current level of performance, a reconfigurable circuit of such complexity is a significant step forward for FSLW technology. We believe that the techniques developed in this work will be used to enable fast and inexpensive fabrication of integrated photonic circuits specifically tuned for particular experiments in the optical laboratory. Fully reconfigurable integrated circuits are prerequisites for modern experiments in quantum optics and linear-optical quantum computing. Thus the results presented in this work may boost the research in this rapidly developing field.

ACKNOWLEDGMENTS

The work is supported by the Russian Science Foundation Project No. 16-12-00017.

APPENDIX A: CHIP PARAMETERS

The geometrical scheme of the integrated multiport interferometer is presented in Fig. 4. The summary of the geometrical parameters of the circuit can be found in Table II. The curvature radius R denotes the radius of the circular waveguide bends.

The waveguides support both horizontally and vertically-polarized eigenmodes. The mode field profiles are presented in Fig. 5. The two-dimensional (2D) Gaussian fit reveals that $w_x = 4.3 \pm 0.1$ μm and $w_y = 5.5 \pm 0.1$ μm for the horizontal-polarization state and $w_x = 4.8 \pm 0.1$ μm and $w_y = 5.9 \pm 0.1$ μm for the vertical-polarization state. If the coupling loss is determined solely by the overlap of the waveguide eigenmodes and the eigenmode of the Nufern 780HP fiber, it may be approximately estimated as 0.05 dB per facet.

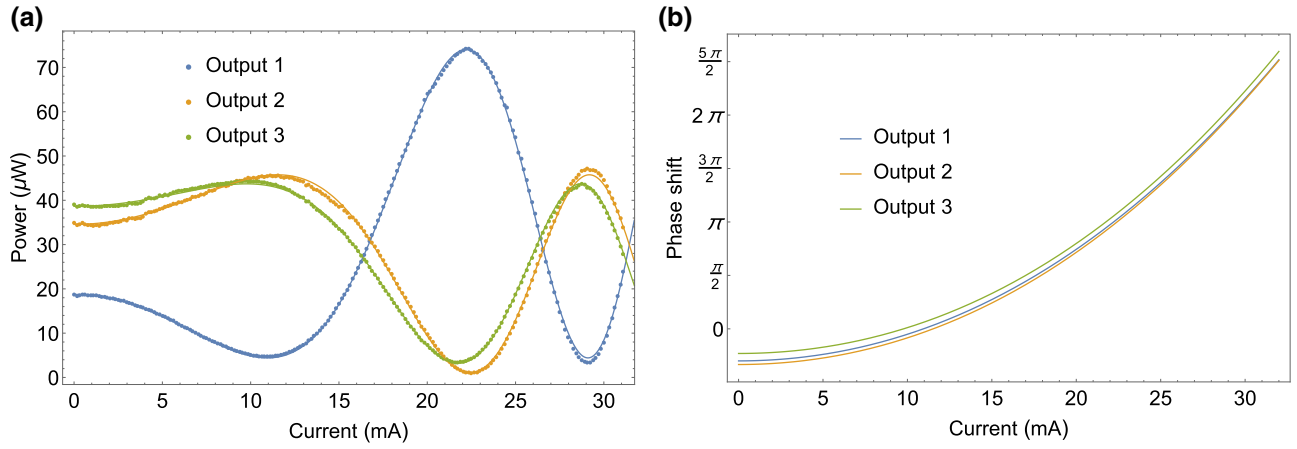

FIG. 7. Phase-calibration plots. (a) The power in different outputs vs the currents through heater h8 are fitted according to model (C1) to estimate the phase introduced. (b) Phases vs current calibration obtained through different fitting of the output port power.

TABLE III. The results of experimental fitting of the calibration for heater h8. Model C1 is used.

	Parameters		
	α (rad)	β (10^{-3} rad/mA^2)	γ (10^{-5} rad/mA^3)
Output 1	-0.942 ± 0.003	7.45 ± 0.03	3.72 ± 0.09
2	-1.046 ± 0.005	7.42 ± 0.06	4.07 ± 0.19
3	-0.724 ± 0.005	7.10 ± 0.04	4.90 ± 0.12

APPENDIX B: NUMERICAL SIMULATIONS

The optimization algorithms were tested in numerical simulations. An experimentally obtained value for the difference function may be calculated from the theoretical values of S_j:

$$S_j = S_{ij} = |U_{ij}|, \tag{B1}$$

where U denotes the unitary matrix describing the transformation performed by the chip in the space of the optical modes. The unitary matrix U is determined by the thermo-optical circuit phases φ_i according to the circuit schematic shown in Fig. 1(b). The thermo-optically induced phase delays may be expressed through the controlling currents I_i as follows:

$$\varphi_i = \sum_{j=1}^{12} \beta_{ij} I_j^2. \tag{B2}$$

Here, we assume that no cross talk between heaters is present, i.e., $\beta_{ij} \neq 0$ only if $i = j$, and no cubic components I_i^3 are used for the simulation purposes. This is justified, since the main goal of the simulation is to tune the parameters of the search algorithms for subsequent usage in the real experiment. This is why the theoretical difference function is just a rough estimate of the experimental one.

1. Noiseless simulations

Three optimization algorithms are compared in this section:

(1) Simultaneous-perturbation stochastic approximation (SPSA) [35]. This algorithm is quite similar to a gradient descent and it is supposed to work well for possibly noisy functions with few local minima. The SPSA algorithm demonstrates poor performance in comparison to the others, so it is excluded from further consideration. The reasons for the bad performance of SPSA can probably be attributed to sticking to local minima.

(2) Particle-swarm optimization (PSO) [36]. Although PSO is known to be a global optimization algorithm, the results are generally unsatisfactory. However, PSO outperforms other algorithms for "noisy" simulations.

(3) Very fast simulated annealing (VFSA) [37]. This procedure shows the best performance and is used to acquire the majority of the data in the experiment.

The evolution of the theoretical difference function $1 - F$ with the number of measurements N for the different optimization algorithms is illustrated in Fig. 6(a). The results are averaged over 1000 runs. The target configuration used here is $\tilde{S} = \{1, 0, 0, 0\}$.

2. Noisy simulations

A simple experimental noise model is tested to compare the optimization algorithms in nonideal noisy conditions. It is assumed that the measured value S_i fluctuates in the following way:

$$S_i' = S_i + \Delta, \tag{B3}$$

where Δ is a uniformly distributed random variable $\Delta \in U(-S_{\text{noise}}, S_{\text{noise}})$; here, S_{noise} determines the noise value. S' is renormalized subsequently.

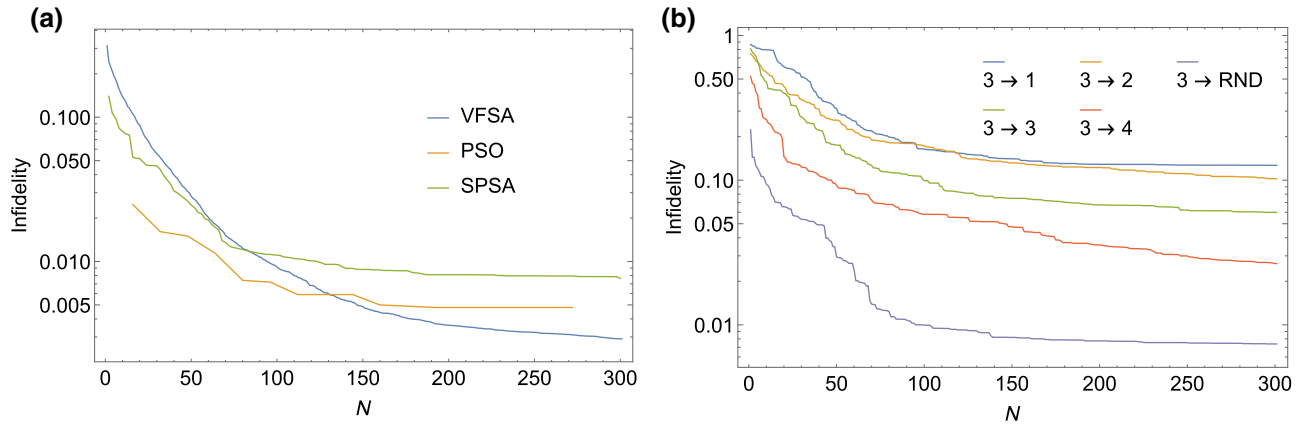

FIG. 8. (a) The cross-talk effect measured by injecting light into port 1, sweeping the driving current of heater h1, and monitoring the output power at port 1. (b) The cross-talk effect measured by injecting the light into port 1, sweeping the driving current of heater h8, and monitoring the output power at port 1.

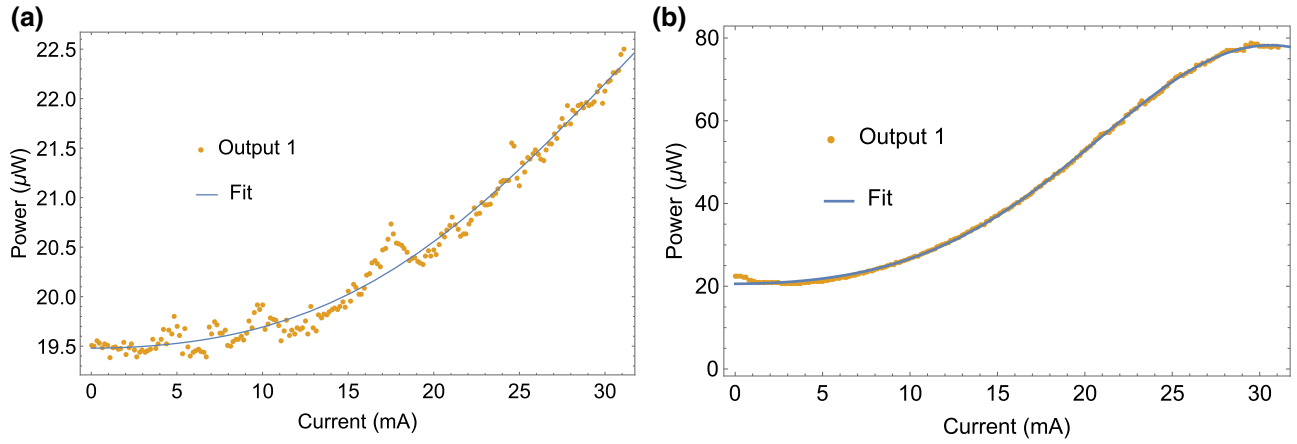

FIG. 9. The experimental results averaged over 10 runs. (a) The dependence of the infidelity on the number of measurements N for the different optimization algorithms. The required output intensity configuration is set to $S_{\text{req}} = \{0.25, 0.25, 0.25, 0.25\}$. (b) The convergence to the different output configurations using VFSA. The input is fixed to port 3. The infidelities are shown for the device operating in switching mode (switching to output ports $1, \ldots, 4$) as well as for convergence to a random output configuration.

The results of the noisy simulations are shown in Fig. 6(b). PSO performs better than VFSA under the influence of noise, so both algorithms are tested in the experiment.

APPENDIX C: PHASE CALIBRATION DETAILS

The phases introduced by the thermo-optical circuit are fitted according to the following model:

$$\phi(I) = \alpha + \beta I^2 + \gamma I^3. \tag{C1}$$

Figure 7(a) presents the data used for phase estimation. The different output port power data for heater h8 are fitted independently and the fit parameters obtained are given in Table III. The final phase vs current calibration curves [given in Fig. 7(b)] are in good agreement.

The cross-talk effects are considered in both the longitudinal and the transverse directions. The transverse cross talk resulting from the effect of, for example, heater h8 on the first interferometer, which is normally driven by heater h2, is expected to be sufficiently larger than the analogous longitudinal effect that is taking place, for example, between heater h1 and the same interferometer. The measurement results for both effects are depicted in Fig. 8. The transverse cross-talk coefficient $\beta_{\text{tr}} = 3.99 \pm 0.14$ rad/mA^2 is approximately 4 times larger than the longitudinal $\beta_{\text{long}} = 1.02$ rad/mA^2, which is comparable to the distance ratio between heaters h2 and h8 ($d_{\text{tr}} = 11.17$ mm) and heaters h2 and h1 [($d_{\text{long}} = 2.52$ mm)], respectively. This serves as evidence that the longitudinal cross talk is mainly of a thermal nature and cannot be attributed to electrical cross talk. The degree of electrical insulation between the adjacent wires could be estimated by measurement of the resistance, which in our case yielded values in excess of 1 MΩ.

APPENDIX D: OTHER EXPERIMENTAL OPTIMIZATION RESULTS

This section is devoted to some experimental results that are not presented in Sec. IV.

1. Comparison of algorithms

After the preliminary parameter tuning with numerical simulations, three optimization algorithms are tested in the experiment for adaptive circuit optimization. The results are shown in Fig. 9(a). The VFSA algorithm proves to show the best convergence among the three optimization algorithms described.

2. Switching convergence

Switching the light from the third input port to one of the output ports appears to be a harder task for the thermo-optical circuit than tuning to a random output configuration $\tilde{S}$. As discussed in Sec. IV, the main reason for this is the background light coupled to every output multimode fiber. This light comes from the scattering on the whole structure of the interferometer. This background noise can be reduced by using an SMF fiber array at the output.

The switching convergence obtained using the VFSA is depicted in Fig. 9(b). The background noise spoils the convergence to any configuration that has a 0 element, e.g., $\tilde{S} = \{0.33, 0, 0.33, 0.34\}$.

[1] Alberto Politi, Martin J. Cryan, John G. Rarity, Siyuan Yu, and Jeremy L. O'Brien, Silica-on-silicon waveguide quantum circuits, Science **320**, 646 (2008).
[2] Hagai B. Perets, Yoav Lahini, Francesca Pozzi, Marc Sorel, Roberto Morandotti, and Yaron Silberberg, Realization of

Quantum Walks with Negligible Decoherence in Waveguide Lattices, Phys. Rev. Lett. **100**, 170506 (2008).

[3] P. J. Shadbolt, M. R. Verde, A. Peruzzo, A. Politi, A. Laing, M. Lobino, J. C. F. Matthews, M. G. Thompson, and J. L. O'Brien, Generating, manipulating and measuring entanglement and mixture with a reconfigurable photonic circuit, Nat. Photonics **6**, 45 (2011).

[4] Jacques Carolan, Christopher Harrold, Chris Sparrow, Enrique Martń-López, Nicholas J. Russell, Joshua W. Silverstone, Peter J. Shadbolt, Nobuyuki Matsuda, Manabu Oguma, Mikitaka Itoh, Graham D. Marshall, Mark G. Thompson, Jonathan C. F. Matthews, Toshikazu Hashimoto, Jeremy L. O'Brien, and Anthony Laing, Universal linear optics, Science **349**, 711 (2015).

[5] Nicholas C. Harris, Gregory R. Steinbrecher, Mihika Prabhu, Yoav Lahini, Jacob Mower, Darius Bunandar, Changchen Chen, Franco N. C. Wong, Tom Baehr-Jones, Michael Hochberg, Seth Lloyd, and Dirk Englund, Quantum transport simulations in a programmable nanophotonic processor, Nat. Photonics **11**, 447 (2017).

[6] Joshua W. Silverstone, Damien Bonneau, Jeremy L. O'Brien, and Mark G. Thompson, Silicon quantum photonics, IEEE J. Sel. Top. Quantum Electron. **22**, 390 (2016).

[7] Alberto Peruzzo, Jarrod McClean, Peter Shadbolt, Man-Hong Yung, Xiao-Qi Zhou, Peter J. Love, Alán Aspuru-Guzik, and Jeremy L. O'Brien, A variational eigenvalue solver on a photonic quantum processor, Nat. Commun. **5**, 4213 (2014).

[8] S. Paesani, A. A. Gentile, R. Santagati, J. Wang, N. Wiebe, D. P. Tew, J. L. O'Brien, and M. G. Thompson, Experimental Bayesian Quantum Phase Estimation on a Silicon Photonic Chip, Phys. Rev. Lett. **118**, 100503 (2017).

[9] Jianwei Wang, Stefano Paesani, Raffaele Santagati, Sebastian Knauer, Antonio A. Gentile, Nathan Wiebe, Maurangelo Petruzzella, Jeremy L. O'Brien, John G. Rarity, Anthony Laing, and Mark G. Thompson, Experimental quantum Hamiltonian learning, Nat. Phys. **13**, 551 (2017).

[10] C. M. Wilkes, X. Qiang, J. Wang, R. Santagati, S. Paesani, X. Zhou, D. A. B. Miller, G. D. Marshall, M. G. Thompson, and J. L. O'Brien, 60 dB high-extinction auto-configured Mach-Zehnder interferometer, Opt. Lett. **41**, 5318 (2016).

[11] Alexander Y. Piggott, Jesse Lu, Konstantinos G. Lagoudakis, Jan Petykiewicz, Thomas M. Babinec, and Jelena Vuckovi ć, Inverse design and demonstration of a compact and broadband on-chip wavelength demultiplexer, Nat. Photonics **9**, 374 (2015).

[12] Nicholas C. Harris, Yangjin Ma, Jacob Mower, Tom Baehr-Jones, Dirk Englund, Michael Hochberg, and Christophe Galland, Efficient, compact and low loss thermo-optic phase shifter in silicon, Opt. Express **22**, 10487 (2014).

[13] Zeqin Lu, Kyle Murray, Hasitha Jayatilleka, and Lukas Chrostowski, in *2016 IEEE Photonics Conference (IPC), Waikoloa, Hawaii, USA* (IEEE, 2016).

[14] Antonio Ribeiro, Alfonso Ruocco, Laurent Vanacker, and Wim Bogaerts, Demonstration of a 4×4-port universal linear circuit, Optica **3**, 1348 (2016).

[15] Daniel Pérez, Ivana Gasulla, Lee Crudgington, David J. Thomson, Ali Z. Khokhar, Ke Li, Wei Cao, Goran Z. Mashanovich, and José Capmany, Multipurpose silicon photonics signal processor core, Nat. Commun. **8**, 636 (2017).

[16] Ken Tanizawa, Keijiro Suzuki, Munehiro Toyama, Minoru Ohtsuka, Nobuyuki Yokoyama, Kazuyuki Matsumaro, Miyoshi Seki, Keiji Koshino, Toshio Sugaya, Satoshi Suda, Guangwei Cong, Toshio Kimura, Kazuhiro Ikeda, Shu Namiki, and Hitoshi Kawashima, Ultra-compact 32×32 strictly-non-blocking Si-wire optical switch with fan-out LGA interposer, Opt. Express **23**, 17599 (2015).

[17] Jie Sun, Erman Timurdogan, Ami Yaacobi, Ehsan Shah Hosseini, and Michael R. Watts, Large-scale nanophotonic phased array, Nature **493**, 195 (2013).

[18] Chen Sun, Mark T. Wade, Yunsup Lee, Jason S. Orcutt, Luca Alloatti, Michael S. Georgas, Andrew S. Waterman, Jeffrey M. Shainline, Rimas R. Avizienis, Sen Lin, Benjamin R. Moss, Rajesh Kumar, Fabio Pavanello, Amir H. Atabaki, Henry M. Cook, Albert J. Ou, Jonathan C. Leu, Yu-Hsin Chen, Krste Asanović, Rajeev J. Ram, Milos A. Popović, and Vladimir M. Stojanović, Single-chip microprocessor that communicates directly using light, Nature **528**, 534 (2015).

[19] Weilin Liu, Ming Li, Robert S. Guzzon, Erik J. Norberg, John S. Parker, Mingzhi Lu, Larry A. Coldren, and Jianping Yao, A fully reconfigurable photonic integrated signal processor, Nat. Photonics **10**, 190 (2016).

[20] Alexander Szameit, Ivan L. Garanovich, Matthias Heinrich, Andrey A. Sukhorukov, Felix Dreisow, Thomas Pertsch, Stefan Nolte, Andreas Tünnermann, and Yuri S. Kivshar, Polychromatic dynamic localization in curved photonic lattices, Nat. Phys. **5**, 271 (2009).

[21] Fulvio Flamini, Lorenzo Magrini, Adil S. Rab, Nicoló Spagnolo, Vincenzo D'Ambrosio, Paolo Mataloni, Fabio Sciarrino, Tommaso Zandrini, Andrea Crespi, Roberta Ramponi, and Roberto Osellame, Thermally reconfigurable quantum photonic circuits at telecom wavelength by femtosecond laser micromachining, Light: Sci. Appl. **4**, e354 (2015).

[22] Simone Atzeni, Adil S. Rab, Giacomo Corrielli, Emanuele Polino, Mauro Valeri, Paolo Mataloni, Nicoló Spagnolo, Andrea Crespi, Fabio Sciarrino, and Roberto Osellame, Integrated sources of entangled photons at the telecom wavelength in femtosecond-laser-written circuits, Optica **5**, 311 (2018).

[23] G. Della Valle, R. Osellame, and P. Laporta, Micromachining of photonic devices by femtosecond laser pulses, J. Opt. A: Pure Appl. Opt. **11**, 013001 (2009).

[24] Giacomo Corrielli, Andrea Crespi, Riccardo Geremia, Roberta Ramponi, Linda Sansoni, Andrea Santinelli, Paolo Mataloni, Fabio Sciarrino, and Roberto Osellame, Rotated waveplates in integrated waveguide optics, Nat. Commun. **5**, 4249 (2014).

[25] I. V. Dyakonov, M. Yu. Saygin, I. V. Kondratyev, A. A. Kalinkin, S. S. Straupe, and S. P. Kulik, Laser-written polarizing directional coupler with reduced interaction length, Opt. Lett. **42**, 4231 (2017).

[26] Fulvio Flamini, Nicoló Spagnolo, Niko Viggianiello, Andrea Crespi, Roberto Osellame, and Fabio Sciarrino, Benchmarking integrated linear-optical architectures for quantum information processing, Sci. Rep. **7**, 15133 (2017).

[27] Mario Arnolfo Ciampini, Adeline Orieux, Stefano Paesani, Fabio Sciarrino, Giacomo Corrielli, Andrea Crespi, Roberta Ramponi, Roberto Osellame, and Paolo Mataloni,

Path-polarization hyperentangled and cluster states of photons on a chip, Light: Sci. Appl. **5**, e16064 (2016).

[28] Zachary Chaboyer, A. Stokes, J. Downes, M. J. Steel, and Michael J. Withford, Design and fabrication of reconfigurable laser-written waveguide circuits, Opt. Express. **25**, 33056 (2017).

[29] Andrea Crespi, Marco Bentivegna, Ioannis Pitsios, Davide Rusca, Davide Poderini, Gonzalo Carvacho, Vincenzo D'Ambrosio, Adán Cabello, Fabio Sciarrino, and Roberto Osellame, Single-photon quantum contextuality on a chip, ACS Photonics **4**, 2807 (2017).

[30] P. L. Mennea, W. R. Clements, D. H. Smith, J. C. Gates, B. J. Metcalf, R. H. S. Bannerman, R. Burgwal, J. J. Renema, W. S. Kolthammer, I. A. Walmsley, and P. G. R. Smith, Modular linear optical circuits, arXiv:1803.04539 [quant-ph].

[31] William R. Clements, Peter C. Humphreys, Benjamin J. Metcalf, W. Steven Kolthammer, and Ian A. Walsmley, Optimal design for universal multiport interferometers, Optica **3**, 1460 (2016).

[32] Michael Reck, Anton Zeilinger, Herbert J. Bernstein, and Philip Bertani, Experimental Realization of any Discrete Unitary Operator, Phys. Rev. Lett. **73**, 58 (1994).

[33] M. J. Weber, *Handbook of Optical Materials* (CRC Press, Boca Raton, Florida, USA, 2003).

[34] Michael Nielsen and Isaac L. Chuang, *Quantum Computation and Quantum Information* (Cambridge University Press, New York, USA, 2010).

[35] James C. Spall, in *Introduction to Stochastic Search and Optimization* (Wiley-Blackwell, Hoboken, New Jersey, USA, 2005), p. 176.

[36] Maurice Clerc, Beyond standard particle swarm optimisation, Int. J. Swarm Intell. Res. 1, **46**, 15133 (2010).

[37] Mohammad-Taghi Vakil-Baghmisheh and Alireza Navarbaf, in *2008 International Symposium on Telecommunications, Piscataway, New Jersey, USA*, August 2008 (IEEE, 2008), p. 61.